We are IntechOpen, the world's leading publisher of Open Access books Built by scientists, for scientists

6,900
Open access books available

186,000
International authors and editors

200M
Downloads

154
Countries delivered to

Our authors are among the

TOP 1%
most cited scientists

12.2%
Contributors from top 500 universities

CLARIVATE ANALYTICS
BOOK CITATION INDEX
INDEXED

WEB OF SCIENCE™

Selection of our books indexed in the Book Citation Index
in Web of Science™ Core Collection (BKCI)

Interested in publishing with us?
Contact book.department@intechopen.com

Numbers displayed above are based on latest data collected.
For more information visit www.intechopen.com

Tip-Enhanced Raman Spectroscopy of 2D Semiconductors

Mahfujur Rahaman and Dietrich R.T. Zahn

Abstract

Two-dimensional (2D) semiconductors are one of the most extensively studied modern materials showing potentials in large spectrum of applications from electronics/optoelectronics to photocatalysis and CO_2 reduction. These materials possess astonishing optical, electronic, and mechanical properties, which are different from their bulk counterparts. Due to strong dielectric screening, local heterogeneities such as edges, grain boundaries, defects, strain, doping, chemical bonding, and molecular orientation dictate their physical properties to a great extent. Therefore, there is a growing demand of probing such heterogeneities and their effects on the physical properties of 2D semiconductors on site in a label-free and non-destructive way. Tip-enhanced Raman spectroscopy (TERS), which combines the merits of both scanning probe microscopy and Raman spectroscopy, has experienced tremendous progress since its introduction in the early 2000s and is capable of local spectroscopic investigation with (sub-) nanometer spatial resolution. Introducing this technique to 2D semiconductors not only enables us to understand the effects of local heterogeneities, it can also provide new insights opening the door for novel quantum mechanical applications. This book chapter sheds light on the recent progress of local spectroscopic investigation and chemical imaging of 2D semiconductors using TERS. It also provides a basic discussion of Raman selection rules of 2D semiconductors important to understand TERS results. Finally, a brief outlook regarding the potential of TERS in the field of 2D semiconductors is provided.

Keywords: TERS, Raman spectroscopy, 2D semiconductors, TMDC, MMC, plasmonics, nanoscale chemical imaging, local heterogeneities

1. Introduction

The ability of isolating stable, atomically thin monolayers of layered materials stimulated a new field of atomic-scale interface physics, with tremendous potential for novel quantum optoelectronic applications [1]. Graphene, the first isolated 2D material consisting of an atomically thin carbon sheet provides much stronger mechanical strength and electrical or heat conductivity compared to its bulk counterpart graphite [2–4]. Thus, graphene was predicted to have great impact on devices with ballistic charge transport or quantum anomalous Hall effect [5]. However, the lack of a bandgap coupled with challenges and consequences associated to the attempts of bandgap opening hinders its application as an active material in

semiconducting devices [6]. In this context, 2D semiconductors have attracted significant attention owing to their suitable bandgap required for optoelectronic applications. Some of these semiconductors already possess carrier mobilities that can outperform existing Si CMOS technology at the scaling limit, although they are affected by some other limiting factors [7]. Therefore, extensive research is going on to gain both fundamental understanding of these materials and to explore new 2D semiconductors for potential applications.

One of the novel aspects of 2D semiconductors is that their optical properties can be tuned as a function of layer number [8]. The most famous 2D semiconductors in this respect are the transition metal dichalcogenides (TMDCs). For example, in bulk TMDCs are indirect bandgap semiconductors, which can be tuned upward ~1 eV with decreasing layer number down to monolayer. More importantly, the nature of the bandgap also changes from indirect to direct at the monolayer thickness [9]. Density functional theory (DFT) predicts that the direct excitonic transition energy at the Brillouin zone (BZ) K point in TMDCs hardly shows any dependence with respect to the layer thickness [9]. However, the indirect transition along the $\Gamma - Q$ (valence band – conduction band) direction (the smallest energy gap in the bulk, *i.e.* the bandgap) increases monotonically as the layer number decreases. Therefore, at monolayer thickness the direct transition becomes smaller than the indirect gap and hence the TMDC becomes a direct bandgap semiconductor. Black phosphorous (BP) also exhibits a similar behavior (from 0.3 eV in bulk to 1.5 eV in monolayer) whereas the nature of the bandgap remains direct due to strong interlayer coupling [10]. Other 2D semiconductors such as, metal monochalcogenides (MMCs) are direct bandgap semiconductors in bulk and turn into indirect bandgap semiconductor at some thicknesses as the layer number decreases [11, 12].

Even though these semiconductors are few atoms thick, some of them can absorb up to 15% of light in the visible range due to strong light-matter interaction [13]. The dramatically reduced dielectric screening in the out-of-plane direction creates strongly bound excitons with binding energies in the range of few hundreds of meV [14, 15]. Therefore, their optical response is dominated by excitons or multi-particle complexes at room temperature (RT) [16, 17]. Atomically flat dangling bond free surfaces of these materials are free from career scattering caused by surface roughness, which can lead to high performance optoelectronic devices with large on–off ratio ($\sim 10^8$), photoresponsivity ($\sim 10^7$ mAW^{-1}), and career mobility (10^3 cm^{2}V^{-1} s^{-1}) at RT [7, 18, 19]. Both few layer BP and InSe based field effect transistors show comparable career mobility (10^3 cm^{2}V^{-1} s^{-1}) at RT suggesting they can outperform Si based CMOS at the scaling limits [20]. However, BP suffers from poor stability in air [21] and the polar nature of InSe leads to layer dependent Fröhlich interaction [22] and thus optical phonon limited career mobility.

For all the extraordinary optoelectronic properties of 2D semiconductors, the influence of local heterogeneities such as edges, grain boundaries, defects, strain, doping, chemical bonding *etc.* are very crucial due to the strong Coulomb screening in these systems [23, 24]. Therefore, a powerful analytical technique, which is capable of studying chemical structures, phase, stress, impurities, molecular interaction *etc.* at the nanoscale, is essential to understand the underlying physics important for device applications. Raman spectroscopy meets all criteria when it comes to measure these heterogeneities at the micro-scale. It has been frequently applied as a non-destructive and straightforward to measure technique to study 2D semiconductors over the last decade [25]. However, the major disadvantages of this technique are its low sensitivity and optical diffraction limited spatial resolution. While typically one in every 10^5–10^7 scattered photons is counted for Raman scattering, the typical spatial resolution of conventional micro-Raman scattering is in the range of 0.5 to 1 μm. Hence, both of these characteristics limit Raman

spectroscopy from acquiring the local heterogeneous information stated above. Therefore, tip-enhanced Raman spectroscopy (TERS) has become a popular analytical technique for studying 2D semiconductors in recent years [26]. It combines the benefits of both scanning probe microscopy (SPM) and Raman spectroscopy, thus permits a very good spatial resolution and high sensitivity for local spectroscopic investigation and chemical imaging. In this chapter, we start with discussing the principle of TERS by explaining the technical aspects of it. Then, recent developments and applications of TERS of 2D semiconductors are discussed. Finally, conclusions and future directions of TERS of 2D semiconductors are addressed.

2. Principle of TERS

Raman scattering is at the core of TERS, which is light inelastically scattered by elementary excitations such as vibrational modes (phonons) in the material probed. Consequently photons are emitted that are shifted in energy with respect to the energy of the exciting light. The shifts are directly correlated to the phonon frequencies of the material. This effect was first observed by C. V. Raman in 1928 and thus named after him [27]. The fundamentals and the various aspects of Raman scattering are comprehensively covered *e.g.* in the book series "Light Scattering in Solids I-IX" [28, 29]. Here, we would like to point out a few facts, which are relevant for TERS. First, the Raman process in matter involves the instantaneous absorption of a photon, excitation of the electronic system, scattering of electron or hole by a vibrational mode or phonon, and relaxation of the excited state accompanied by the emission of a photon. This higher order process has an extremely weak Raman scattering cross section (typically 10^{-26}–10^{-31} cm^2) [30, 31]. The intensity of the inelastically scattered Raman light is thus orders of magnitude weaker than the elastically scattered Rayleigh light, which imposes the need of strong reduction of the elastically scattered light by the Raman spectrometers. The weakness of Raman scattering is especially critical if the amount of matter and/or the available scattering volume are very small as is the case for low-dimensional structures such as quantum dots or 2D semiconductors. For such samples, enhancement mechanisms are employed. An important one is resonance enhancement, for which the exciting light is tuned to a real electronic transition of the sample leading to strong optical absorption and consequently stronger Raman scattering (typically two orders of magnitude). However, this may not be sufficient for low-dimensional systems and thus further enhancement *e.g.* by using surface-enhanced Raman scattering (SERS) is required. SERS has seen tremendous increase in applications in recent years [32]. Compared to conventional Raman cross sections SERS cross section can be up to ten orders of magnitude larger allowing *e.g.* single molecule detection [33–35]. SERS uses metallic nanostructures to create a very strong electric field via localized surface plasmon resonances (LSPR) or lightening rod effects also known as plasmonic effects [36]. Besides a local electromagnetic (EM) field enhancement, photo-driven charge transfer (CT) mechanisms can also lead to an additional enhancement factor of up to 10^3 [34]. Despite the remarkable improvement compared to conventional Raman scattering, SERS still suffers from the optically diffraction limit and is restricted to resolve spatial chemical information beyond 200 nm [26]. TERS can also be esteemed as the ultimate case of SERS with the SPM tip acting as the single metallic nanostructure enhancing the Raman cross section. The photon emitted in the Raman process is shifted in energy with respect to the photon energy of the exciting light towards higher (anti-Stokes) or lower energy (Stokes) by the energy of the elementary excitation (phonon) depending on whether a phonon is absorbed or emitted. The Stokes-shifted part of the Raman

spectrum is predominantly probed in Raman experiments. As the Raman shift directly reflects the energy of the elementary excitation (phonon), it can directly be used to identify materials. Moreover, the intensity (under non-resonant conditions) is related to the number of scatterers (scattering volume), while the energy position and the lineshape can be influenced by parameters such as temperature, strain, doping, and crystallinity. Finally, the Raman scattering process obeys symmetry selection rules, which are represented by the so-called Raman tensors (derivative of the polarization tensors with respect to the phonon elongation). By choosing the polarization of the incident and scattered light it is possible to probe distinct components of the Raman tensor. The Raman selection rules can be altered by *e.g.* electric fields, strain, and by reduced dimensionality as well as by the presence of the SPM tip inducing strong electric field gradients.

TERS works using the same principal as SERS, *i.e.* it utilizes the plasmonic enhancement around a sharp metallic tip. However, unlike SERS it employs a single SPM tip to collect local phonon information by taking advantage of the lateral resolution of SPM [37, 38]. When excited by a suitable photon energy, the collective oscillation of the conduction band electrons in the sharp metallic tip amplifies and confines the optical field in the vicinity of the tip apex. The resulting enhancement of the EM field then produces Raman scattering from a nanoscopic volume of the sample under the apex. The general schematic of the TERS mechanism is shown in **Figure 1a**. For simplification the tip apex can be assumed as shown in the schematic to be a metal sphere acting as the metal nanostructure prerequisite for the plasmonic enhancement. When an EM wave with E field parallel to the tip long axis excites the tip, a strong plasmonic field (also known as local electric field or simply local field) is created around the apex since the metal nanostructure can facilitate both LSPR and lightening rod effect. A finite element method (FEM) simulation of the plasmonic field enhancement around the Au tip apex with a radius of 10 nm at 638 nm excitation is presented in **Figure 1b**. The local field amplitude is enhanced by a factor of 5 at the tip apex. Since, the Raman scattering is approximately proportional to the fourth power of the excitation field, TERS can thus amplify the local Raman information by a factor of 625 under these simulated conditions.

The lightning rod effect is introduced by the anisotropy of the tip geometry (the larger the anisotropy, the stronger the field enhancement) and thus independent of the excitation wavelength. However, the LSPR is created due to the collective oscillation of conduction band electrons at the metal surface. Therefore, several factors influence the LSPR energy and oscillator strength, such as material, size, shape, and dielectric interface [36, 39, 40]. Gold and silver are the two most widely used noble metals for TERS tips. Both metals reveal small dielectric loss, stability in air, and tunability of the LSPR in the visible spectrum. Importantly, they both have some advantages and disadvantages, which become critical deciding factors for
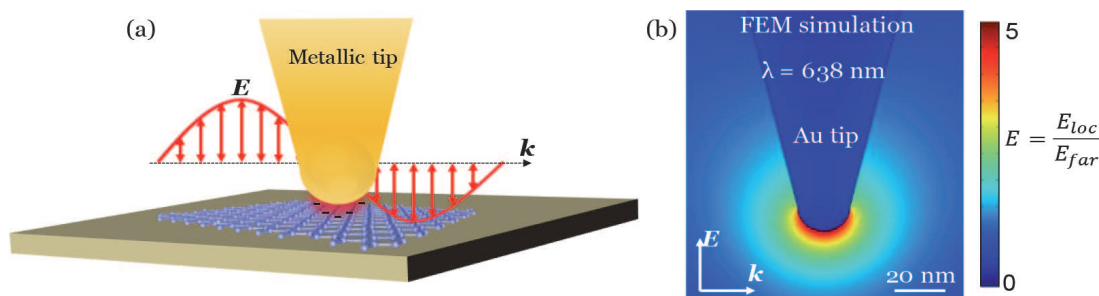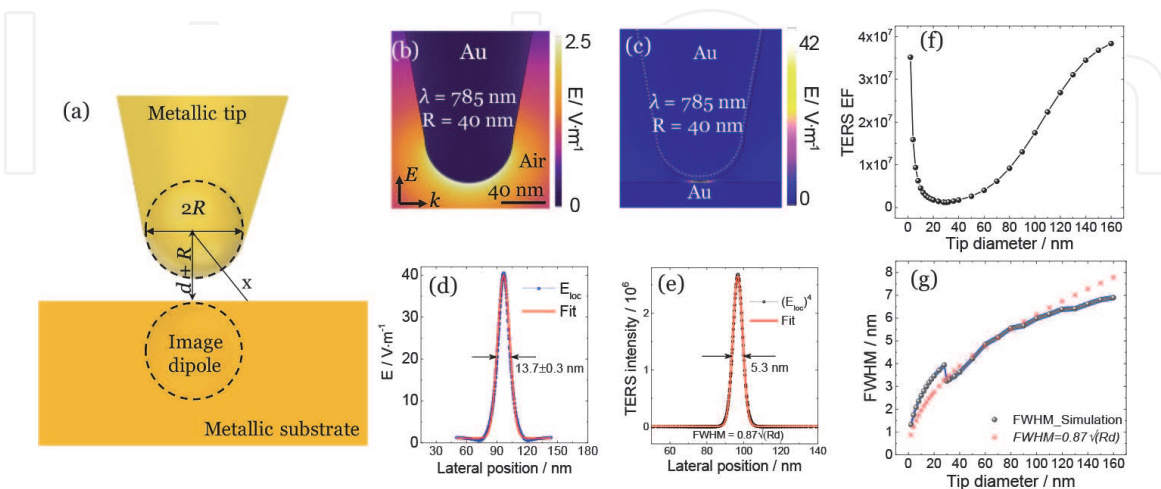

Figure 1.
Schematic representation of TERS (a) and FEM simulation of the plasmonic field enhancement at the tip apex for an Au tip (b).

TERS applications. For example, silver shows a more pronounced plasmonic effect but gold provides a better environmental stability. Thus, the latter makes gold the more popular material for TERS tips. Additionally, for the same size and shape of the apex, the LSPR of a tip made of Ag lies at a higher energy than that of an Au tip [36]. Therefore, Ag tips are more commonly in use for green excitation and Au tips are more suitable for red and near-IR TERS applications.

The TERS schematic shown in **Figure 1a** is also known as conventional TERS, in which the local electric field is created by the tip dipole oscillation. The TERS sensitivity (*i.e.* enhancement factor, EF, and spatial resolution, SR) is moderate in a conventional TERS geometry. Hence, a usual practice of increasing TERS sensitivity multifold is to introduce a metal substrate, which then creates an image dipole inside the substrate [41]. Thus, the combined tip-substrate system acts as a dimer and enhances the sensitivity to a great extent such that the EF can reach more than three order of magnitude higher values than that in the conventional TERS [42]. This way of enhancing the TERS sensitivity is also known as gap-mode TERS configuration.

Figure 2a displays the schematic of the gap-mode TERS configuration. The strength of the dimer coupling and consequently the gap-mode TERS sensitivity depend on the tip-substrate distance d. A comparison of generated local electric field distribution around an Au tip apex in conventional TERS and gap-mode TERS is presented in **Figure 2b** and **c**. As can be seen, the enhancement of the local electric field amplitude in the case of conventional TERS is almost 20 times smaller than that in the gap-mode TERS configuration. The spatial resolution of gap-mode TERS is also superior to that of the conventional TERS. The full width at half maximum (FWHM) of the local electric field E_{loc} distribution around the tip apex in conventional TERS is proportional to ($\sim 1.345(R + d)$), where R is the tip radius and d is the distance between the sample surface and the tip apex [41]. However, in the case of gap-mode TERS the FWHM of the E_{loc} distribution is given by $2\sqrt{Rd}$ as shown in **Figure 2d** [37]. Since the TERS intensity is proportional to the fourth power of E_{loc}, the TERS SR also turns out to be much smaller than that in the conventional geometry. The analysis of SR can be performed using the schematic shown in **Figure 2a**. The potential drop between the tip sphere and the image sphere can be written as $\Delta V = |E_{loc}|d$; whereas the potential difference between two

Figure 2.
Schematic of the gap-mode TERS configuration (a). Comparison of local electric field distribution between conventional (b) and gap-mode TERS (c). Local electric field amplitude (d) and TERS enhancement (e) in a gap-mode configuration shown in (c) calculated for a tip-substrate distance of 1 nm. TERS EF (f) and SR (g) in a gap-mode TERS configuration as a function of tip diameter. The tip-substrate distance was kept at 1 nm. Figure (a) to (e) reproduced from ref. [37] with permission from the Royal Society of Chemistry and (f) and (g) from ref. [38].

sites in the absence of the these two spheres can be expressed as $\Delta V = |E_0|(2R + d)$, E_0 is the incident field. Since, the spheres are equipotential, we can thus write

$$\left. \begin{array}{l} \Delta V = |E_0|(2R + d) = |E_{loc}|d \\[2mm] |E_{loc}| = \dfrac{2R + d}{d} E_0 \end{array} \right\} \tag{1}$$

For a certain tip-substrate geometry both R and d are fixed at the smallest distance from the tip apex to the sample surface being d, which is along the center of the electric field lines. Therefore, the lateral offset of the electric field from the center can be written as [38].

$$|E_{loc}(x)| = \frac{\Delta V}{2R + d - 2\sqrt{R^2 - x^2}} \tag{2}$$

For the TERS intensity Eq. (2) becomes

$$|E_{loc}(x)|^4 = \left(\frac{\Delta V}{2R + d - 2\sqrt{R^2 - x^2}} \right)^4 \tag{3}$$

At $x = 0$, $|E_{loc}|^4$ has a maximum of $\left(\Delta V / d \right)^4$. Hence, at half maximum we can write

$$2d^4 = \left(2R + d - 2\sqrt{R^2 - x^2} \right)^4 \tag{4}$$

For a very small d and $R >> d$, we can neglect the terms containing d^2. Thus, the SR of gap-mode TERS becomes

$$SR = 2\sqrt{\left(\sqrt[4]{2} - 1 \right) Rd} \approx 0.87\sqrt{Rd} \tag{5}$$

A more detailed theoretical study of the TERS enhancement and spatial resolution in gap-mode TERS as a function of tip diameter is shown in **Figure 2f–g**. The tip-substrate distance d was kept fixed at 1 nm in the simulation. Both the calculated TERS EF and SR under 638 nm excitation show two distinctive regimes, one below and the other above a tip size of 28 nm. The sharp increase of the TERS EF and SR below 28 nm of the tip diameter is due to the lightning rod effect. On contrary, the slow increment of both EF and SR above 28 nm is the result of the LSPR of the tip apex. The red asterisks in the SR graph (**Figure 2g**) represent the results of Eq. (5) in very good agreement to the SR calculated from the LSPR contribution of the tip apex. Eq. (5) clearly indicates that for a given tip radius both EF and SR can be amplified by reducing the distance d. However, at very small d, the quantum mechanical effects such as non-local screening effects and electron tunneling weaken the TERS sensitivity and impose an unavoidable limiting factor avoiding a singularity at $d = 0$ [43, 44].

3. Surface selection rules of TERS in 2D semiconductors

According to the FEM simulations, the overall electric field intensity beneath the tip apex is zero for an incident beam polarized along the XY plane as shown in **Figure 3a**. Therefore, for an incident beam polarized along the z-direction (along the tip long axis) the intensity enhancement matrix can be written as [26].
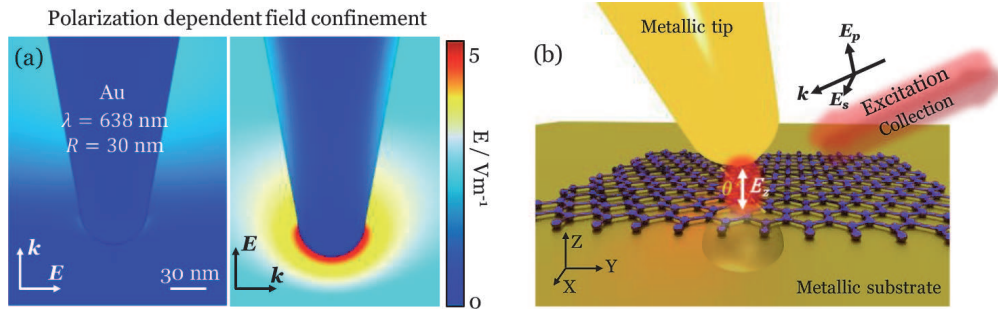
Figure 3.
Incident light polarization dependent E_{loc} *distribution around the tip apex (a). Schematic of the gap-mode TERS in the side-illumination geometry (b). The dashed line projects the normal to the basal plane of 2D semiconductor at any given geometrical situation, which is inclined at an angle θ to the z-axis.*

$$G = \begin{pmatrix} G_{xx} & 0 & 0 \\ 0 & G_{yy} & 0 \\ 0 & 0 & G_{zz} \end{pmatrix} \approx \begin{pmatrix} 0 & 0 & 0 \\ 0 & 0 & 0 \\ 0 & 0 & G_{zz} \end{pmatrix} \qquad (6)$$

The above enhancement condition is also applicable for the gap-mode TERS configuration. Hence, for a side-illumination geometry at an incident angle, which satisfies the tip polarization condition, a tip in gap-mode TERS configuration confines and enhances the E_{loc} along z-direction as shown in **Figure 3b**. Thus, the TERS intensity can be expressed as

$$I_{TERS} \propto \left| G_{\omega_{in}} \cdot \alpha'_{zz} \cdot G_{\omega_{sc}} \right|^2 \qquad (7)$$

$G_{\omega_{in}}$ and $G_{\omega_{sc}}$ are the intensity enhancement matrices for incident and scattered light. α'_{zz} is the Raman tensor involved in a vibrational mode along the z-direction, which can be derived from the 3 x 3 matrix of the anisotropic polarizability tensor associated to the phonon vibrations as follows

$$\alpha = \begin{pmatrix} \alpha_{xx} & \alpha_{xy} & \alpha_{xz} \\ \alpha_{yx} & \alpha_{yy} & \alpha_{yz} \\ \alpha_{zx} & \alpha_{zy} & \alpha_{zz} \end{pmatrix} \qquad (8)$$

The idea of surface selection rules was first conceptualized by Moskovits on flat metallic surfaces [45]. Due to the adsorption of molecules on a flat metal surface, they will experience a different electric field, since incident light is reflected off the metal substrate. Assuming both s- and p-polarized incident light causing Raman scattering, the scattered radiation at any given angle of incidence, ϕ consists of superposition of two waves as given by [45]

$$\left. \begin{aligned} E'_s &= (1 + r'_s)p_x \\ E'_p &= p_y\left(1 - r'_p\right)\cos\phi' + p_z\left(1 + r'_p\right)\sin\phi' \end{aligned} \right\} \qquad (9)$$

The primes are associated to the scattered radiation, r_s and r_p are the respective Fresnel reflection coefficient, and p_i is the polarization inside the molecule expressed by $p = \alpha E$, where α can be derived from Eq. (8). The four components associated to the Raman experiment are ss, sp, ps, and pp, the first and second letters refer to the incident and scattered light polarization, respectively. In the limit of a very good reflector, all the components except pp reduce to zero, since $r_s \approx -1$ and $r_p \approx 1$. Therefore, the effective Raman scattering intensity becomes

$$I_{sc}^{eff} \approx \left| \alpha'_{zz} \left(1 + r_p\right)\left(1 + r'_p\right) \right|^2 \sin^2 \phi \, \sin^2 \phi' \tag{10}$$

According to Eq. (10) the effective Raman scattering depends on the z-component of the Raman tensor, normally not measured in ordinary Raman spectroscopy. However, in the gap-mode TERS configuration the coupling between the phonon with tensor elements having z-component and the E_{loc} changes the TERS intensity dramatically leading to so-called TERS selection rules.

In a real situation, the normal to the 2D material basal plane is parallel to the direction of E_{loc} (*i.e.* $\theta = 0$ in **Figure 3b**) in a Raman backscattering geometry. Therefore, one can expect that the TERS signal is only associated to the α'_{zz} component. However, if the normal to the 2D basal plane is tilted by an angle θ due to local structural deformation, other components of the Raman tensor also contribute to the overall TERS response.

It is also worth noting that above mentioned assumption is a simplified model, which does not consider interface chemistry. For example, in the case of chemisorption the molecular geometry or orientation may alter significantly leading to the breaking of the Raman selection rules. In such cases, some Raman inactive modes can become Raman active [46]. Moreover, light-plasmon coupling in a nanocavity between the tip and the metal substrate can lead to the alteration of classical Raman selection due to photon tunneling through perturbation of the evanescent field [47].

In polarization dependent Raman measurements we observe the scattered light intensity as a function of polarization directions of both the incident and scattered light. The Raman intensity can be written as

$$I \propto \left| e_s \mathcal{R} e_i \right|^2 \tag{11}$$

Here, e_s and e_i are the unit vectors of the electric field of the scattered and incident light and $\mathcal{R}$ is a second rank tensor also called Raman tensor derived from Eq. (8). There is plenty of literature including text books available discussing polarization and Raman tensors in conventional Raman measurements [25, 50–52]. In this chapter, we revisit the Raman tensors of first order Raman modes in 2D semiconductors, which are important to understand the TERS selection rules. Group theory analysis tells us that the Raman active phonon modes belong to the irreducible representations, the basis function of which contain quadratic terms of x, y, z. Thus, to have non-zero Raman intensity at a given e_s and e_i geometry, $\mathcal{R}$ should have a non-zero matrix element. The Raman tensors of three first order Raman modes in 2D semiconductors (D_{3h} point group) are presented below [25, 50].

$$\left.\begin{aligned} R(E', xy) &= \begin{pmatrix} 0 & d & 0 \\ d & 0 & 0 \\ 0 & 0 & 0 \end{pmatrix} \\ R(E', x^2 - y^2) &= \begin{pmatrix} -c & 0 & 0 \\ 0 & -c & 0 \\ 0 & 0 & 0 \end{pmatrix} \\ R(A'_1, x^2 + y^2 \,\text{and}\, z^2) &= \begin{pmatrix} a & 0 & 0 \\ 0 & a & 0 \\ 0 & 0 & b \end{pmatrix} \end{aligned}\right\} \tag{12}$$
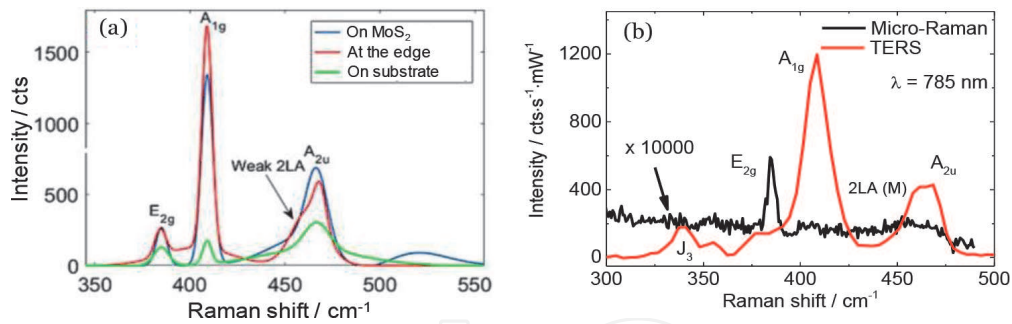
Figure 4.
TERS spectra of few layer MoS₂ deposited on an Au coated glass slide acquired using 638 nm excitation (a). Micro-Raman and TERS spectra of monolayer MoS₂ deposited on an Au nanodisc array on a Si substrate acquired using 785 nm excitation (b). The micro-Raman spectrum was obtained over an area of ∼1 μm² (spot size) and the TERS spectrum was taken locally on top of Au nanodisc with a spatial resolution of 2.3 nm. In both cases, together with the A_{1g} Raman mode, the infra-red active A_{2u} is enhanced significantly. Figure (a) is adapted from ref. [48] (Copyright © 2017, IEEE) and (b) is adapted from ref. [49] with permission from the Royal Society of Chemistry.

There is one more doubly degenerate Raman mode with E'' (E_{1g}) symmetry available in 2D semiconductors, which is forbidden in backscattering geometry. Therefore, the discussion of this mode is omitted here. Interested readers can learn more about this phonon feature in this review [50]. From Eq. (12) it is clear that the out-of-plane, A_1' (A_{1g}) phonon mode has a Raman tensor component along z-direction (α_{zz}'). Therefore, the A_1' Raman mode is strongly sensitive to the TERS geometry. Since other modes are active in cross polarization geometry, they can still be observed in side-illumination TERS configuration, even though the TERS intensity is not as enhanced as for the out-of-plane Raman mode. An experimental demonstration of TERS selection rules on MoS₂ is shown in **Figure 4** [48, 49]. In the case of few layer MoS₂ on an Au surface and resonantly excited by a 638 nm laser the far-field contribution on the substrate close to the flake shows comparable intensity of the in-plane E_{2g} and out-of-plane A_{1g} mode (**Figure 4a**). However, as the tip approaches the flake, the out-of-plane A_{1g} mode enhances significantly [48]. Similarly, a marked TERS enhancement of the A_{1g} mode is observed from the monolayer MoS₂ deposited on Au nanodisc arrays on Si substrate and excited by 785 nm excitation (**Figure 4b**). Due to the below bandgap excitation (bandgap of monolayer MoS₂ is ∼660 nm) only the in-plane E_{2g} mode is observed in micro-Raman spectra. In contrast, TERS spectra of monolayer MoS₂ on Au nanodisc show a significant modification with a giant enhancement of the A_{1g} mode. Together with other factors (as discussed later in this chapter), the TERS selection rules amplify multifold the out-of-plane phonon modes [49].

Another important aspect of TERS selection rules is demonstrated by the enhancement of the infra-red (IR) active out-of-plane A_{2u} mode in both works. As shown in **Figures 2** and **3**, the tip-substrate dimer system creates a strong dipole moment in the nanocavity (or even sub-nanocavity) resulting in a strong out-of-plane E_{loc}. Therefore, IR active phonon modes, which induce a transition dipole moment parallel to the E_{loc}, can also be strongly enhanced. Since the IR active A_{2u} phonon vibration creates a transition dipole moment perpendicular to the MoS₂ basal plane, it couples to the E_{loc} at the tip-substrate nanocavity polarized along z-direction. This is remarkable since the A_{2u} phonon mode is Raman forbidden and only observed in resonant Raman conditions. Therefore, Voronine *et al.* [48] could still see this mode on the substrate as a far field contribution. However, the strong plasmonic field created at the tip-nanodisc nanocavity is able to not only excite this Raman forbidden IR mode, but also amplify it significantly under non-resonant 785 nm excitation as shown in **Figure 4b** [49].

4. Local phonon properties in 2D semiconductors

4.1 Strain induced local bandgap modulation

Strain plays an important role in manipulating optoelectronic properties of 2D semiconductors. The remarkable strength of 2D semiconductors such as TMDCs compared to other conventional semiconductors makes them well suited for straintronic applications. For example, a MoS_2 monolayer can sustain a large biaxial strain >10%; whereas bulk silicon usually breaks at a strain of ~1.5% [53]. This extraordinary property of 2D semiconductors has led to burgeoning research of strain engineered optoelectronic properties in recent times [53–55]. Among them, most of the studies provide macro/microscale information of strain induced opto-electronic manipulation using conventional optical spectroscopy. In contrast, the local modification of band structures due to spatially inhomogeneous strain distri-bution on the nanoscale is much less explored. Like the band structure, phonons in 2D semiconductors are directly affected by a wide range of parameters including strain [56, 57]. Therefore, Raman spectroscopy, one of the most frequently used non-destructive spectroscopies, becomes a powerful technique to investigate the different components of strain and their effect on optoelectronic properties of these semiconductors. Due to energy and momentum conservation, phonons participat-ing in first order Raman scattering processes need to satisfy the wavevector condition $q \approx 0$ (*i.e.* near the Γ point in the crystal). Though, phonons with non-zero q can also contribute to the Raman signals. However, they require two or more scattering processes assisted by a real electronic transition, a process called resonant-Raman scattering [58]. Hence, monitoring both the first order and the higher order Raman modes can provide quantitative knowledge of strain and its impact on the electronic structure of 2D semiconductors. Additionally, both tip enhanced photoluminescence (TEPL) and TERS can be performed simultaneously and can be used as complementary techniques to investigate local strain effects on the excitonic response. Though, special care needs to be taken to interpret the results since PL intensity, lineshape, and spectral position also depend on other local heterogeneities [24].

The two well-studied first order Raman modes in TMDCs are in-plane E_{2g} and out-of-plane A_{1g}. Using the combination of both experiments and *ab initio* calcula-tions shows that the in-plane E_{2g} mode is more sensitive to uni- or bi-axial strain than the out-of-plane A_{1g} mode [56, 60]. TERS reveals similar behavior for multi-layer and monolayer TMDCs when probing highly localized strain at the nanoscale. Rahaman *et al.* studied local strain heterogeneities in 3 L MoS_2 caused by a nano-structured gold substrate using TERS with a spatial resolution of less than 25 nm [59]. TERS measurements were performed in a side-illumination geometry under 638 nm excitation. When deposited on hexagonal periodic arrays of gold nanotriangles, 3 L MoS_2 underwent local deformations on top and in between the nanotriangles as shown in **Figure 5a**. Hence, this is an ideal system to study the local flexibility at the nanoscale. Looking at the AFM topography and the 2nd order derivative of it, which represents the local curvature image (**Figure 5b**), it is clear that a variety of deformations caused strain inhomogeneities in MoS_2. The center of the valley is unstrained and the twisted areas between two gold nanotriangles is most strained. The corresponding TERS map together with selective TERS spectra of the MoS_2/Au heterostructure are presented in **Figure 5c** and **d**. As explained in the previous section the out-of-plane A_{1g} mode is found to be more enhanced than the in-plane E_{2g} mode due to TERS selection rules. After deconvoluting all the spectra using voigt functions, the frequency shift of the in-plane E_{2g} mode agrees
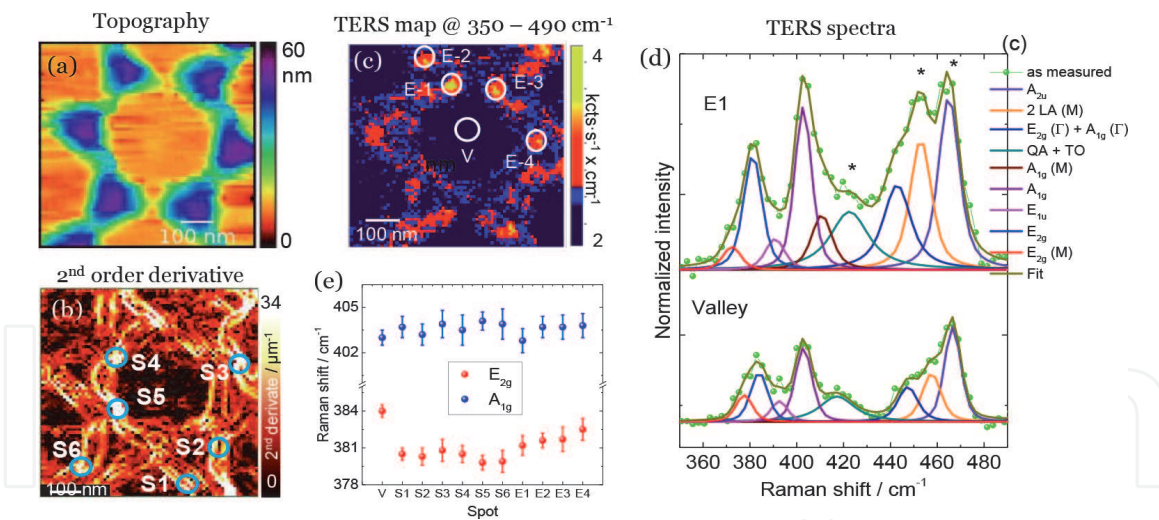
Figure 5.
AFM topography (a) and 2nd order derivative of the topography (b). Both topography and 2nd derivative images show heterogeneous biaxial strain distribution in 3 L MoS₂. The corresponding TERS map created for the spectral range of 350–490 cm⁻¹ (c) and two representative TERS spectra (d) taken from two respective areas shown in (c). Site dependent peak position of two first order Raman modes for the quantification of strain (e). Adapted from ref. [59] (Copyright © 2017 American Chemical Society).

well with the local curvature image and a maximum strain of 1.4% is determined in the twisted regions from the frequency shift of 4.2 cm^{-1}. However, at the corner of the nanotriangles the strain is calculated to be ~0.9% from a frequency shift of 2.6 cm^{-1} of the E_{2g} mode. The same authors then studied monolayer MoS$_2$ on top of gold nanodiscs and observed a similar amount of strain at the rim of the discs [49].

It is important to note that the above described TERS experiments were performed in resonant Raman condition with 638 nm excitation (excitation close to the A optical transition in MoS$_2$) [61]. Therefore, there are as many as seven Raman features observed in the TERS spectra together with the two first order Raman modes (E_{2g} and A_{1g}). The Raman band around 378 cm^{-1} is the in-plane $E_{2g}(M)$ [62]. However, some reports argued that Davydov splitting of the in-plane $E_{2g}(\Gamma)$ should appear around this frequency position as well [13]. The feature around 390 cm^{-1} is a Raman inactive E_{1u} excited due to the resonant Raman condition in the TERS configuration [63]. The Raman mode around 410 cm^{-1} is an out-of-plane A_{1g} phonon in the vicinity of the M point of the BZ and analogous to the mode $E_{2g}(M)$. The frequency around 420 cm^{-1} is attributed to a two phonon process involving a successive emission of a dispersive longitudinal quasi-acoustic (QA) phonon and a dispersionless transverse optical (TO) phonon along the c-axis [64]. The broad feature around 450 cm^{-1} is a convolution of minimum three modes. The first one around 440 cm^{-1} is $E_{2g}(\Gamma) + A_{1g}(\Gamma)$ [62]. The frequency centered around 450 cm^{-1} involves two phonons of the longitudinal acoustic branch with opposite momenta at the M point of BZ (2LA (M)) [65], and the third feature around 460 cm^{-1} is the infrared active A_{2u} mode as discussed in the previous section.

The rich variety of second order Raman features in MoS$_2$ in resonant Raman condition also yields important information about its physical properties and the electronic band structure. Zhang *et al*. performed similar TERS experiments on monolayer MoS$_2$ deposited on gold nanopyramids and by combining TERS and TEPL they probed the nanoscale variation of the electronic band structure induced by strain [60]. Under resonance excitation, a few of the second order Raman features in MoS$_2$ were assigned to longitudinal acoustic (LA) and/or transverse acoustic (TA) phonons. These Raman bands scatter light through intervalley resonant scattering of the excited electrons by phonons when excited near the B exciton

energy. The process is known as double resonance Raman scattering (DRRS) and is similar to the process that leads to the creation of the *D* and 2*D* band in graphene/ graphite [66, 67]. The DRRS process is explained by the schematic shown in **Figure 6a**. After the excitation of an e-h pair near the *K* valley of BZ, the excited electron is inelastically scattered from *K* to the *K'* valley by the emission of a phonon. In the relaxation process the excited electron is then inelastically scattered back to the *K* valley by the emission of a second phonon, where the e-h pair recombines and emits a photon. In MoS$_2$, the Raman mode around 420 cm^{-1} and the 2*LA* mode around 450 cm^{-1} are the results of DRRS processes. Zhang *et al.* observed that together with the shift in peak position of these second order features, the peak intensities are also inhomogeneously modified due to local strain [60]. Their DFT calculations of the phonon dispersion for acoustic branches show that DRRS processes are sensitive to the changes in the momentum and energy conservation constraints that govern which transitions and states in the BZ participate in the resonant interactions. Thus any distortion in the band structure caused by strain is reflected in the DRRS processes. With positive hydrostatic strain, the calculated phonon dispersion indicates a negative shift in peak position for both *LA* and *TA* modes at the *K* point in the BZ due to increasing lattice constants. On the other hand, the increase in peak areas associated to the DRRS processes depends on the relative position of the conduction band minima at the *K* and *Q* point in the BZ. In an unstrained monolayer MoS$_2$, the *K* point conduction band minima is lower in energy than the *Q* point conduction band minima. Therefore, the *K* − *K'* transition mediated by the $q_{\sim K}$ acoustic phonons are much more prominent than the *K* − *Q* transition mediated by $q_{\sim M}$ phonons. However, when tensile strain is applied, the difference in energy between the *K* and *Q* point conduction band minima decreases. Hence, more transitions mediated by the $q_{\sim M}$ phonons satisfy the constraints on a DRRS process, which in turn increases the respective peak area.

Like externally induced strain via transferring TMDCs monolayers on nanostructured substrates as discussed above, direct evaporation of a metal, for example gold on monolayer MoS$_2$, can cause large strain ($\sim$ 5%) at the interface due to lattice mismatch. Combining various SPM techniques and TERS Jo *et al.* demonstrated that
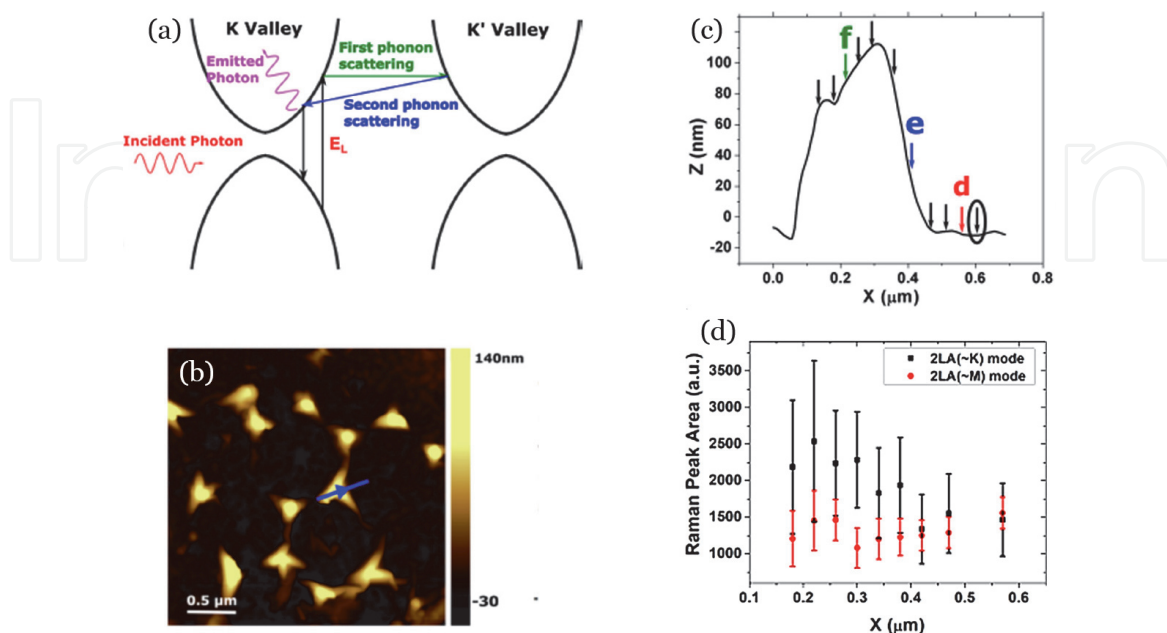
Figure 6.
Illustration of the DRRS process in 2D semiconductors (a). AFM topography of monolayer MoS$_2$ deposited on gold NTs (b). A line profile is created from the topography along the dashed line and presented in (c). Integrated Raman peak area of the DRRS triggered 2LA mode in MoS$_2$ (d) taken at the arrow positions along the line profile shown in (c). Adapted from ref. [60] (© 2018 American Physical Society).

large tensile strain induced at the interface in this process reduces the bandgap of MoS_2 and thus influences the contact resistance as a consequence [68].

TERS has become a powerful technique to probe local strain variation in 2D semiconductors, which in turn helps us to understand the inhomogeneities in optoelectronic response of these materials.

4.2 Effect of variance in atomic registry on electronic properties

The reduced dimensionality of 2D semiconductors makes them susceptible to structural variations near the internal and external boundaries. Parameters, such as impurities, defects, and grain boundaries interfere strongly with intrinsic properties resulting in highly inhomogeneous optoelectronic response [23, 69, 70]. While conventional optical spectroscopy leaves a confusing picture regarding the effect of these heterogeneities [71], near-field optical studies can help us to understand the correlation of local structural heterogeneities with nano-optical response. In recent years, the combination of TEPL and TERS has been successfully introduced to investigate these heterogeneities. In TMDCs, the out-of-plane A_{1g} Raman mode is particularly sensitive to changes in carrier concentration (or doping) via strong electron–phonon coupling [72]. Therefore, by comparing the peak positions of both in-plane E_{2g} and out-of-plane A_{1g} modes it is possible to separate the local doping effect from other heterogeneities [49]. Additionally, the Raman intensity of the out-of-plane A_{1g} mode is also affected by the physical and chemical irregularities such as doping, atomic vacancies, bond strain, grain boundaries (GB) at the atomic level [73]. Understanding the variations of atomic registries are especially important for 2D semiconductors as Park et al. showed that the excitonic behavior differs at the edges, nucleation sites (NS), and twin boundaries (TB) [24]. Using the combination of TERS, TEPL, and atomic force local strain microscopy they studied the PL response of PVD grown WSe_2 and the results suggest that the defect concentration and stoichiometry of W and Se atoms in different sites can result in different excitonic mechanisms.

Due to their extraordinary physical properties, many groups are now synthesizing 2D semiconductors by CVD and other deposition techniques with the vision of industry scale production. However, in terms of crystal quality these deposition processes still require further optimization to be able to use them in electronic applications. CVD grown 2D semiconductors often reveal several structural heterogeneities as discussed in this section. Therefore, proper understanding is the key for the optimization of the deposition process and hence improving the crystal quality. While confocal micro-Raman spectroscopy is unable to obtain locally heterogeneous information, TERS can uncover them with nanometer precision. Smithe et al. studied the growth mechanism, GB, and defects in CVD grown monolayer $MoSe_2$ using TERS [74]. Their investigation revealed that CVD $MoSe_2$ monolayers have nano-domains of MoO_3, which are invisible in confocal Raman spectroscopy. They also observed that the TERS intensity was strongly suppressed at GBs, which was attributed to the fast degradation of the GBs in ambient conditions due to the presence of higher defect concentration.

For optoelectronic devices the physics of semiconductor–metal interfaces is critical, since they are at the core of charge separation and collection. Jariwala et al. directly probed interfaces between WSe_2 and noble metals such as gold and silver to investigate the influence of intrinsic doping on electronic properties using the cross-correlated spatial mapping of contact potential difference (CPD), photocurrent, TERS, and TEPL [75]. Their TERS map acquired with 638 nm excitation showed two distinct regions with domains of 10–100 nm lateral size, which correlated with

CPD images as well. The regions of lower CPD exhibited non-resonant TERS spectra with a single Raman mode around 250 cm^{-1}. This single Raman band corresponds to the combination of E_{2g} and A_{1g} modes of WSe$_2$. In contrast, TERS spectra representing higher CPD regions exhibited resonant Raman scattering with a number of additional features. It is important to note that the laser line 638 nm overlaps with the broad shoulder on the high-energy side of the A exciton in WSe$_2$. Therefore, Raman spectra acquired with this laser line induces resonant Raman response in this material with a number of additional peaks including DRR features, which are not observed with other excitation wavelengths. Later, by performing photocurrent measurement they observed that both higher and lower CPD areas generated higher photocurrents, but with opposite signs. Therefore, they concluded that the areas showing resonant Raman behavior are intrinsically n-type, while non-resonant areas are p-type.

4.3 Semiconducting to metallic phase transition

The stable crystal structure of TMDCs is the 2H semiconducting phase. However, these materials are known to form also metallic 1T or 1T' phases (though not stable) due to high density of charge donation or electron doping [76, 77]. Due to strong light matter interaction TMDC monolayers, when integrated with plasmonic antennas, show great potential via modulation of their optoelectronic properties [78]. Generated hot electrons from plasmonic nanostructures can be injected into the conduction band of these 2D semiconductors due to favorable Schottky barrier heights at the interface and a large oscillator strength of these hot electrons [22, 79]. The concept of the doping induced structural phase change is illustrated in **Figure 7a**. According to the crystal field theory, the semiconducting 2H phase consists of M (M = Mo/W) outermost d orbitals of a D_{3h}- MX$_6$ (X = S, Se) unit into three groups creating the stable 2H lattice structure [80]. The doping via hot electrons first destabilizes the 2H phase and induces a splitting of the metal
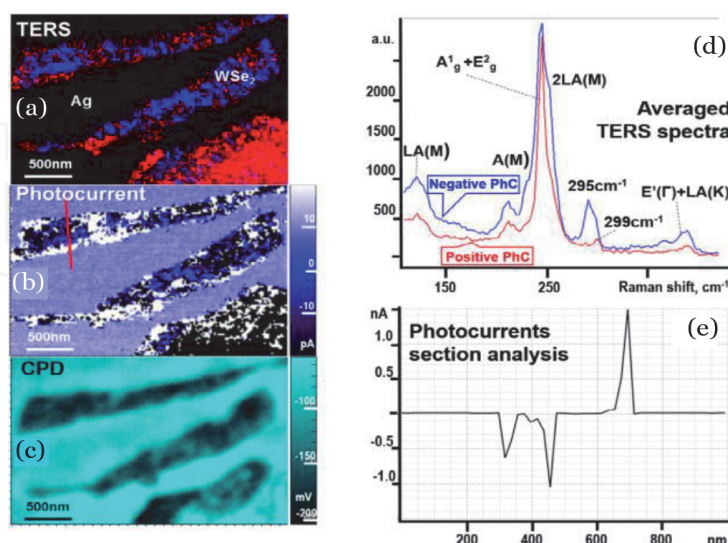
Figure 7.
Single layer flakes of WSe$_2$ exfoliated onto template stripped silver. Combined TERS map (intensity of 295 cm^{-1} peak in blue and of the 250 cm^{-1} ($A_{1g} + E_{2g}$) peak in red) (a). Photocurrent map at zero bias voltage collected simultaneously with TERS map (b), CPD image of the same area (c) and averaged TERS spectra showing resonant and non-resonant behavior (d). Section analysis of the photocurrent map again showing that the value of the photocurrent generated over differently doped domains was similar in absolute value, but of the opposite direction (e). The image is reproduced from ref. [75] (© 2018 IOP Publishing Ltd).

outermost d orbitals to form metallic O_h-MX_6 units into two groups as shown in **Figure 7a** [81–83]. The unoccupied orbitals then accommodate the extra electrons crossing the Schottky barrier (**Figure 8**).

Milekhin *et al.* studied the extremely localized site dependent transient reversible $2H$ to $1T$ phase change in monolayer MoS_2 using TERS. Monolayer MoS_2 was deposited on periodic arrays of gold nanodiscs, thus sandwiched between the nanodisc and the tip to conduct this experiment [49]. Hence, the tip-nanodisc system creates a strongly coupled dimer, which then pumps a high concentration of electrons into the conduction band of MoS_2. As demonstrated by the high resolution TERS images and later by FEM simulations by Rahaman *et al.* [37] the coupling is the strongest between the tip and the rim of the nanodiscs. Therefore, the rim of the nanodiscs became the strongest source of hot electron doping in MoS_2, which consequently showed the transition from the $2H$ to $1T$ phase via the appearance of an additional Raman mode in TERS spectra. Metallic MoS_2 has three additional Raman modes around 156, 226, and 333 cm^{-1} known as J_1, J_2, and J_3, respectively [84]. Due to strong increasing Rayleigh background, Milekhin *et al.* [49] were able to observe only the J_3 Raman mode around 333 cm^{-1}. As can be seen in **Figure 7b**, the transition from $2H$ to $1T$ is extremely site dependent with an area limited by the spatial resolution, which was ~ 2 nm.

4.4 Probing edge related properties

TMDCs have two distinct edges in the form of armchair and zigzag, which possess different electronic properties. For example, the zigzag edge in MoS_2 is metallic, whereas the armchair is semiconducting [85]. Therefore, quantitative measurements or characterization of these edges are important for effective edge engineering, especially for edge contacts for electronic device applications. Huang *et al.* studied edge related properties of atomically thin MoS_2 using TERS [69]. Their local Raman measurements aided by strong plasmonic enhancement of either gold or silver tips probed different Raman features of the edge defects in mono- and bilayer MoS_2 corresponding to the unique lattice vibration and electronic properties of the respective edge.

A broad Raman feature around 220 cm^{-1} was observed along the edges (full of dangling bonds) and absent on the wrinkles and main body (**Figure 9a**). The peak was assigned to the defect (dangling bonds) induced acoustic *LA* with a DRRS feature as explained in Section 4.1. More interestingly, the TERS spectra taken along
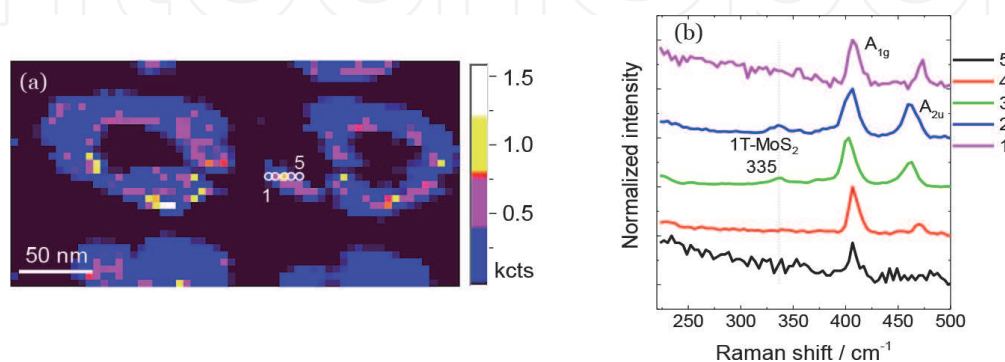
Figure 8.
High resolution TERS map of monolayer MoS$_2$ on gold nanodiscs acquired with a gold tip and 785 nm excitation (a). Corresponding TERS spectra along the circles shown in the map (b). Thanks to the very high spatial resolution the structural phase change from 2H to 1T due to highly localized plasmonic hot electron doping can be observed. The image is reproduced from ref. [49] with permission from the Royal Society of Chemistry.
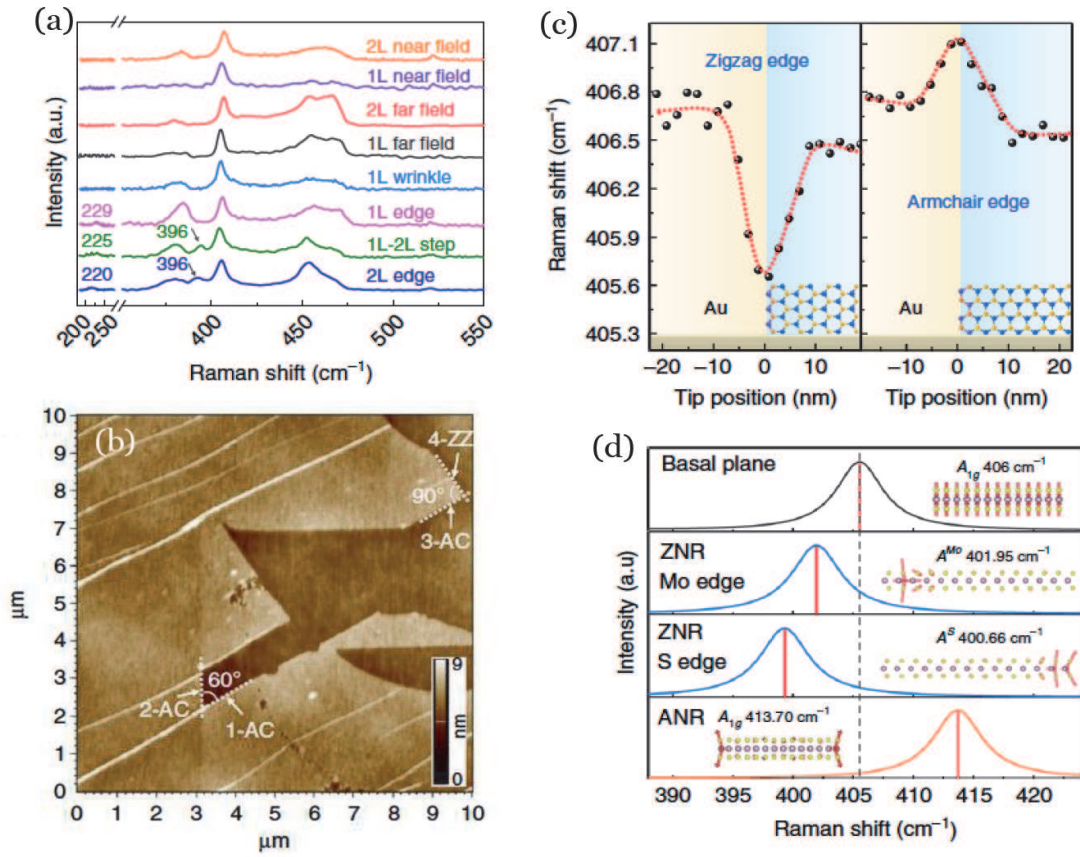
Figure 9.
TERS of mono- and bilayer MoS₂ acquired along the edges and the step between mono- and bilayer (a). AFM topography of a monolayer MoS₂ showing different terminated edges (b). Fitted peak position of A_{1g} mode acquired along a line crossing both zigzag and armchair edges (c). DFT calculated Raman spectra of at different sites in MoS₂ (d). Reproduced from ref. [69].

the edges of the bilayer and the step between mono- and bilayer exhibits an additional feature around 396 cm^{-1}. This particular feature is explicitly observed in bulk at cryogenic temperature and assigned to the $LA(M) + TA(M)$ acoustic mode [86]. This Raman mode involves a DRRS process between the K and Q valleys with wavevector $\boldsymbol{q}_M$ and thus the Raman cross section of this mode depends on the relative energy position of the conduction band minima at the K and Q points in the BZ. Since in bulk the conduction band minima at the Q point is lower than the K point, the Raman scattering efficiency of this mode becomes larger. Therefore, this mode is absent in the basal plane of mono- and bilayer MoS₂. However, along the edges, especially in the case of bilayer MoS₂ the modification of the electronic band structure leads to the considerable lowering of the conduction band energy at the Q point resulting in the activation of the DRRS process of the $LA(M) + TA(M)$ mode.

Another important observation of this study is the edge dependent local Raman sensitivity. The frequency position of the out-of-plane A_{1g} mode showed either upward or downward shift compared to the basal plane when probed along the armchair or zigzag edges, respectively. The AFM topography of monolayer MoS₂ presented in **Figure 9b** shows edges terminated with different angles. For an angle of 60° both edges have the same structure (either armchair or zigzag) and for an angle of 90° the edges are different. The TERS spectra acquired along a line crossing both zigzag and armchair edges show a clear pattern, namely that the A_{1g} mode downshifts at one of the edges and upshifts at other one (**Figure 9c**). According to the DFT calculations the local strain introduced by the two edge structures cause this opposite direction of the frequency shift as shown in **Figure 9d**.

5. Conclusion and outlook

TERS has developed into a versatile characterization technique for a wide range of materials. In recent years we have witnessed chemical mapping of single molecules with a spatial resolution of the bond length using TERS. For 2D semiconductors, an excellent SR of $\sim$2 nm in TERS helped us to understand local heterogeneous behavior of monolayer MoS_2 and demonstrate its tremendous capabilities. In this chapter, we explained the basic principal of TERS and described the surface selection rules in regards to the 2D semiconductors important for understanding the near-field Raman spectra. We also reviewed the recent progress of this technique in the 2D semiconductor field. The potential of TERS certainly guarantees new breakthroughs in the 2D semiconductor field in the near future. One of the recent direction of 2D semiconductors is to create heterostacks like Lego, which promises exotic physics due to the creation of moiré superlattices. The size of a moiré unit cell varies from nm to few 10s nm depending on the lattice mismatch and rotation angle. The moiré superlattice forces the constituent monolayers into phonon renormalization, also known as moiré phonons. TERS can be used to probe these moiré phonons, thus resolving the moiré supercell critical for understanding the moiré physics. Besides, there is a lot of information yet to be resolved on how local heterogeneities control the optical response such as strain induced exciton funneling, defects induced excitonic response, or single photon emitters *etc*. in 2D semiconductors, for which TERS can be a powerful tool to achieve a thorough understanding.

Acknowledgements

Conflict of interest

The authors declare no conflict of interest.

Author details

Mahfujur Rahaman* and Dietrich R.T. Zahn
Semiconductor Physics, Technische Universität Chemnitz, Chemnitz, Germany

*Address all correspondence to: mahfujur.rahaman@physik.tu-chemnitz.de

IntechOpen

References

[1] Wang Q H, Kalantar-Zadeh K, Kis A, Coleman J N and Strano M S 2012 Electronics and optoelectronics of two-dimensional transition metal dichalcogenides *Nature Nanotechnology* 7 699-712

[2] Geim A K and Novoselov K S 2007 The rise of graphene *Nature Materials* 6 183-191

[3] Lee C, Wei X, Kysar J W and Hone J 2008 Measurement of the Elastic Properties and Intrinsic Strength of Monolayer Graphene *Science* 321 385

[4] Seol J H, Jo I, Moore A L, Lindsay L, Aitken Z H, Pettes M T, Li X, Yao Z, Huang R, Broido D, Mingo N, Ruoff R S and Shi L 2010 Two-Dimensional Phonon Transport in Supported Graphene *Science* 328 213

[5] Högl P, Frank T, Zollner K, Kochan D, Gmitra M and Fabian J 2020 Quantum Anomalous Hall Effects in Graphene from Proximity-Induced Uniform and Staggered Spin-Orbit and Exchange Coupling *Physical Review Letters* 124 136403

[6] Jiao L, Zhang L, Wang X, Diankov G and Dai H 2009 Narrow graphene nanoribbons from carbon nanotubes *Nature* 458 877-880

[7] Bandurin D A, Tyurnina A V, Yu G L, Mishchenko A, Zólyomi V, Morozov S V, Kumar R K, Gorbachev R V, Kudrynskyi Z R, Pezzini S, Kovalyuk Z D, Zeitler U, Novoselov K S, Patanè A, Eaves L, Grigorieva I V, Fal'ko V I, Geim A K and Cao Y 2017 High electron mobility, quantum Hall effect and anomalous optical response in atomically thin InSe Nature Nanotechnology 12 223-227

[8] Mak K F, Lee C, Hone J, Shan J and Heinz T F 2010 Atomically Thin MoS$_2$: A New Direct-Gap Semiconductor Physical Review Letters 105 136805

[9] Splendiani A, Sun L, Zhang Y, Li T, Kim J, Chim C-Y, Galli G and Wang F 2010 Emerging Photoluminescence in Monolayer MoS$_2$ *Nano Letters* 10 1271-5

[10] Xu Y, Shi Z, Shi X, Zhang K and Zhang H 2019 Recent progress in black phosphorus and black-phosphorus-analogue materials: properties, synthesis and applications *Nanoscale* 11 14491-527

[11] Rahaman M, Bejani M, Salvan G, Lopez-Rivera S A, Pulci O, Bechstedt F and Zahn D R T 2018 Vibrational properties of GaSe: a layer dependent study from experiments to theory *Semiconductor Science and Technology* 33 125008

[12] Sun Y, Luo S, Zhao X-G, Biswas K, Li S-L and Zhang L 2018 InSe: a two-dimensional material with strong interlayer coupling *Nanoscale* 10 7991-7998

[13] Tonndorf P, Schmidt R, Böttger P, Zhang X, Börner J, Liebig A, Albrecht M, Kloc C, Gordan O, Zahn D R T, Michaelis de Vasconcellos S and Bratschitsch R 2013 Photoluminescence emission and Raman response of monolayer MoS$_2$, MoSe$_2$, and WSe$_2$ *Opt. Express* 21 4908-4916

[14] Chernikov A, Berkelbach T C, Hill H M, Rigosi A, Li Y, Aslan O B, Reichman D R, Hybertsen M S and Heinz T F 2014 Exciton Binding Energy and Nonhydrogenic Rydberg Series in Monolayer WS$_2$ *Physical Review Letters* 113 076802

[15] Zhu B, Chen X and Cui X 2015 Exciton Binding Energy of Monolayer WS$_2$ *Scientific Reports* 5 9218

[16] Mak K F, He K, Lee C, Lee G H, Hone J, Heinz T F and Shan J 2013

Tightly bound trions in monolayer MoS_2 *Nature Materials* 12 207-11

[17] Drüppel M, Deilmann T, Krüger P and Rohlfing M 2017 Diversity of trion states and substrate effects in the optical properties of an MoS_2 monolayer *Nature Communications* 8 2117

[18] Illarionov Y Y, Smithe K K H, Waltl M, Knobloch T, Pop E and Grasser T 2017 Improved Hysteresis and Reliability of MoS_2 Transistors With High-Quality CVD Growth and Al_2O_3 Encapsulation *IEEE Electron Device Letters* 38 1763-6

[19] Buscema M, Groenendijk D J, Blanter S I, Steele G A, van der Zant H S J and Castellanos-Gomez A 2014 Fast and Broadband Photoresponse of Few-Layer Black Phosphorus Field-Effect Transistors *Nano Letters* 14 3347-3352

[20] Feng W, Zheng W, Gao F and Hu P 2017 Atomically thin InSe: A high mobility two-dimensional material *Science China Technological Sciences* 60 1121-1122

[21] Island J O, Steele G A, Zant H S J v d and Castellanos-Gomez A 2015 Environmental instability of few-layer black phosphorus *2D Materials* 2 011002

[22] Rahaman M, Aslam M A, He L, Madeira T I and Zahn D R T 2021 Plasmonic hot electron induced layer dependent anomalous Fröhlich interaction in InSe *Communications Physics* 4 172

[23] Chow P K, Jacobs-Gedrim R B, Gao J, Lu T-M, Yu B, Terrones H and Koratkar N 2015 Defect-Induced Photoluminescence in Monolayer Semiconducting Transition Metal Dichalcogenides *ACS Nano* 9 1520-1527

[24] Park K-D, Khatib O, Kravtsov V, Clark G, Xu X and Raschke M B 2016 Hybrid Tip-Enhanced Nanospectroscopy and Nanoimaging of Monolayer WSe_2 with Local Strain Control *Nano Letters* 16 2621-7

[25] Tan P-H 2019 *Raman Spectroscopy of Two Dimensional Materials*: *Springer Series in Materials Science*, vol. 276, Springer

[26] Shao F and Zenobi R 2019 Tip-enhanced Raman spectroscopy: principles, practice, and applications to nanospectroscopic imaging of 2D materials *Analytical and Bioanalytical Chemistry* 411 37-61

[27] Raman C V 1928 A Change of Wavelength in Light Scattering *Nature* 121 619-

[28] Cardona M 1995 *Light Scattering in Solids: Topics in Applied Physics*, vol 8: Springer, Berlin, Heidelberg

[29] Manuel Cardona R M 2007 *Light scatteriing in Solid IX*: *Topics in Applied Physics*, Springer, Berlin, Heidelberg

[30] Penney C M, Goldman L M and Lapp M 1972 Raman Scattering Cross Sections *Nature Physical Science* 235 110-112

[31] Aggarwal R L, Farrar L W, Saikin S K, Aspuru-Guzik A, Stopa M and Polla D L 2011 Measurement of the absolute Raman cross section of the optical phonon in silicon *Solid State Communications* 151 553-556

[32] Samir Kumar P K, Anamika Das and Chandra Shakher Pathak 2020 *Surface-Enhanced Raman Scattering: Introduction and Applications*: IntechOpen

[33] Blackie E J, Le Ru E C and Etchegoin P G 2009 Single-Molecule Surface-Enhanced Raman Spectroscopy of Nonresonant Molecules *Journal of the American Chemical Society* 131 14466-14472

[34] Langer J, Jimenez de Aberasturi D, Aizpurua J, Alvarez-Puebla R A,

Auguié B, Baumberg J J, Bazan G C, Bell S E J, Boisen A, Brolo A G, Choo J, Cialla-May D, Deckert V, Fabris L, Faulds K, García de Abajo F J, Goodacre R, Graham D, Haes A J, Haynes C L, Huck C, Itoh T, Käll M, Kneipp J, Kotov N A, Kuang H, Le Ru E C, Lee H K, Li J-F, Ling X Y, Maier S A, Mayerhöfer T, Moskovits M, Murakoshi K, Nam J-M, Nie S, Ozaki Y, Pastoriza-Santos I, Perez-Juste J, Popp J, Pucci A, Reich S, Ren B, Schatz G C, Shegai T, Schlücker S, Tay L-L, Thomas K G, Tian Z-Q, Van Duyne R P, Vo-Dinh T, Wang Y, Willets K A, Xu C, Xu H, Xu Y, Yamamoto Y S, Zhao B and Liz-Marzán L M 2020 Present and Future of Surface-Enhanced Raman Scattering *ACS Nano* 14 28-117

[35] Le Ru E C and Etchegoin P G 2009 *Principles of Surface-Enhanced Raman Spectroscopy,* ed E C Le Ru and P G Etchegoin (Amsterdam: Elsevier) pp 185-264

[36] Rahaman M, Moras S, He L, Madeira T I and Zahn D R T 2020 Fine-tuning of localized surface plasmon resonance of metal nanostructures from near-Infrared to blue prepared by nanosphere lithography *Journal of Applied Physics* 128 233104

[37] Rahaman M, Milekhin A G, Mukherjee A, Rodyakina E E, Latyshev Alexander V, Dzhagan V M and Zahn D R T 2019 The role of a plasmonic substrate on the enhancement and spatial resolution of tip-enhanced Raman scattering *Faraday Discussions* 214 309-323

[38] He L, Rahaman M, Madeira T I and Zahn D R T 2021 Understanding the Role of Different Substrate Geometries for Achieving Optimum Tip-Enhanced Raman Scattering Sensitivity *Nanomaterials* 11

[39] Hulteen J C, Treichel D A, Smith M T, Duval M L, Jensen T R and Van Duyne R P 1999 Nanosphere Lithography: Size-Tunable Silver Nanoparticle and Surface Cluster Arrays *The Journal of Physical Chemistry B* 103 3854-3863

[40] Murray W A, Suckling J R and Barnes W L 2006 Overlayers on Silver Nanotriangles: Field Confinement and Spectral Position of Localized Surface Plasmon Resonances *Nano Letters* 6 1772-1777

[41] Richard-Lacroix M, Zhang Y, Dong Z and Deckert V 2017 Mastering high resolution tip-enhanced Raman spectroscopy: towards a shift of perception *Chemical Society Reviews* 46 3922-3944

[42] Kumar N, Su W, Veselý M, Weckhuysen B M, Pollard A J and Wain A J 2018 Nanoscale chemical imaging of solid–liquid interfaces using tip-enhanced Raman spectroscopy *Nanoscale* 10 1815-1824

[43] Savage K J, Hawkeye M M, Esteban R, Borisov A G, Aizpurua J and Baumberg J J 2012 Revealing the quantum regime in tunnelling plasmonics *Nature* 491 574-577

[44] Esteban R, Borisov A G, Nordlander P and Aizpurua J 2012 Bridging quantum and classical plasmonics with a quantum-corrected model *Nature Communications* 3 825

[45] Moskovits M 1982 Surface selection rules The Journal of Chemical Physics 77 4408-4416

[46] Chen X, Liu P, Hu Z and Jensen L 2019 High-resolution tip-enhanced Raman scattering probes sub-molecular density changes *Nature Communications* 10 2567

[47] Poliani E, Wagner M R, Vierck A, Herziger F, Nenstiel C, Gannott F, Schweiger M, Fritze S, Dadgar A, Zaumseil J, Krost A, Hoffmann A and Maultzsch J 2017 Breakdown of

Far-Field Raman Selection Rules by Light–Plasmon Coupling Demonstrated by Tip-Enhanced Raman Scattering *The Journal of Physical Chemistry Letters* 8 5462-5471

[48] Voronine D V, Lu G, Zhu D and Krayev A 2017 Tip-Enhanced Raman Scattering of MoS2 *IEEE Journal of Selected Topics in Quantum Electronics* 23 138-43

[49] Milekhin A G, Rahaman M, Rodyakina E E, Latyshev A V, Dzhagan V M and Zahn D R T 2018 Giant gap-plasmon tip-enhanced Raman scattering of MoS2 monolayers on Au nanocluster arrays *Nanoscale* 10 2755-63

[50] Saito R, Tatsumi Y, Huang S, Ling X and Dresselhaus M S 2016 Raman spectroscopy of transition metal dichalcogenides *Journal of Physics: Condensed Matter* 28 353002

[51] Loudon R 1964 The Raman effect in crystals Advances in Physics 13 423-482

[52] Yu P Y and Cardona M 2010 *Fundamentals of Semiconductors: Physics and Materials Properties,* ed P Y Yu and M Cardona, Springer Berlin Heidelberg, pp 345-426

[53] Peng Z, Chen X, Fan Y, Srolovitz D J and Lei D 2020 Strain engineering of 2D semiconductors and graphene: from strain fields to band-structure tuning and photonic applications *Light: Science & Applications* 9 190

[54] Deng S, Sumant A V and Berry V 2018 Strain engineering in two-dimensional nanomaterials beyond graphene *Nano Today* 22 14-35

[55] Dadgar A M, Scullion D, Kang K, Esposito D, Yang E H, Herman I P, Pimenta M A, Santos E J G and Pasupathy A N 2018 Strain Engineering and Raman Spectroscopy of Monolayer Transition Metal Dichalcogenides *Chemistry of Materials* 30 5148-5155

[56] Lloyd D, Liu X, Christopher J W, Cantley L, Wadehra A, Kim B L, Goldberg B B, Swan A K and Bunch J S 2016 Band Gap Engineering with Ultralarge Biaxial Strains in Suspended Monolayer MoS$_2$ *Nano Letters* 16 5836-41

[57] Frisenda R, Drüppel M, Schmidt R, Michaelis de Vasconcellos S, Perez de Lara D, Bratschitsch R, Rohlfing M and Castellanos-Gomez A 2017 Biaxial strain tuning of the optical properties of single-layer transition metal dichalcogenides *npj 2D Materials and Applications* 1 10

[58] Loudon R 1965 Theory of the resonance Raman effect in crystals J. Phys. France 26 677-683

[59] Rahaman M, Rodriguez R D, Plechinger G, Moras S, Schüller C, Korn T and Zahn D R T 2017 Highly Localized Strain in a MoS2/Au Heterostructure Revealed by Tip-Enhanced Raman Spectroscopy *Nano Letters* 17 6027-33

[60] Zhang Z, De Palma A C, Brennan C J, Cossio G, Ghosh R, Banerjee S K and Yu E T 2018 Probing nanoscale variations in strain and band structure of MoS$_2$ on Au nanopyramids using tip-enhanced Raman spectroscopy *Physical Review B* 97 085305

[61] Chakraborty B, Matte H S S R, Sood A K and Rao C N R 2013 Layer-dependent resonant Raman scattering of a few layer MoS2 *Journal of Raman Spectroscopy* 44 92-6

[62] Peña-Álvarez M, del Corro E, Morales-García Á, Kavan L, Kalbac M and Frank O 2015 Single Layer Molybdenum Disulfide under Direct Out-of-Plane Compression: Low-Stress Band-Gap Engineering *Nano Letters* 15 3139-3146

[63] Molina-Sánchez A and Wirtz L 2011 Phonons in single-layer and few-layer

MoS_2 and WS_2 *Physical Review B* 84 155413

[64] Sekine T, Uchinokura K, Nakashizu T, Matsuura E and Yoshizaki R 1984 Dispersive Raman Mode of Layered Compound 2H-MoS_2 under the Resonant Condition *Journal of the Physical Society of Japan* 53 811-8

[65] Pimenta M A, del Corro E, Carvalho B R, Fantini C and Malard L M 2015 Comparative Study of Raman Spectroscopy in Graphene and MoS_2-type Transition Metal Dichalcogenides Accounts of Chemical Research 48 41-47

[66] Ni Z, Liu L, Wang Y, Zheng Z, Li L-J, Yu T and Shen Z 2009 G-band Raman double resonance in twisted bilayer graphene: Evidence of band splitting and folding *Physical Review B* 80 125404

[67] Carvalho B R, Wang Y, Mignuzzi S, Roy D, Terrones M, Fantini C, Crespi V H, Malard L M and Pimenta M A 2017 Intervalley scattering by acoustic phonons in two-dimensional MoS_2 revealed by double-resonance Raman spectroscopy *Nature Communications* 8 14670

[68] Jo K, Kumar P, Orr J, Anantharaman S B, Miao J, Motala M J, Bandyopadhyay A, Kisslinger K, Muratore C, Shenoy V B, Stach E A, Glavin N R and Jariwala D 2021 Direct Optoelectronic Imaging of 2D Semiconductor–3D Metal Buried Interfaces *ACS Nano* 15 5618-30

[69] Huang T-X, Cong X, Wu S-S, Lin K-Q, Yao X, He Y-H, Wu J-B, Bao Y-F, Huang S-C, Wang X, Tan P-H and Ren B 2019 Probing the edge-related properties of atomically thin MoS_2 at nanoscale *Nature Communications* 10 5544

[70] Fan X, Siris R, Hartwig O, Duesberg G S and Niklaus F 2020 Rapid and Large-Area Visualization of Grain Boundaries in MoS_2 on SiO_2 Using Vapor Hydrofluoric Acid *ACS Applied Materials & Interfaces* 12 34049-57

[71] Ogletree D F, Schuck P J, Weber-Bargioni A F, Borys N J, Aloni S, Bao W, Barja S, Lee J, Melli M, Munechika K, Whitelam S and Wickenburg S 2015 Revealing Optical Properties of Reduced-Dimensionality Materials at Relevant Length Scales *Advanced Materials* 27 5693-5719

[72] Chakraborty B, Bera A, Muthu D V S, Bhowmick S, Waghmare U V and Sood A K 2012 Symmetry-dependent phonon renormalization in monolayer MoS_2 transistor *Physical Review B* 85 161403

[73] Kato R, Umakoshi T, Sam R T and Verma P 2019 Probing nanoscale defects and wrinkles in MoS_2 by tip-enhanced Raman spectroscopic imaging *Applied Physics Letters* 114 073105

[74] Smithe K K H, Krayev A V, Bailey C S, Lee H R, Yalon E, Aslan Ö B, Muñoz Rojo M, Krylyuk S, Taheri P, Davydov A V, Heinz T F and Pop E 2018 Nanoscale Heterogeneities in Monolayer MoSe2 Revealed by Correlated Scanning Probe Microscopy and Tip-Enhanced Raman Spectroscopy *ACS Applied Nano Materials* 1 572-9

[75] Jariwala D, Krayev A, Wong J, Robinson A E, Sherrott M C, Wang S, Liu G-Y, Terrones M and Atwater H A 2018 Nanoscale doping heterogeneity in few-layer WSe_2 exfoliated onto noble metals revealed by correlated SPM and TERS imaging *2D Materials* 5 035003

[76] Ambrosi A, Sofer Z and Pumera M 2015 2H → 1T phase transition and hydrogen evolution activity of MoS2, MoSe2, WS2 and WSe2 strongly depends on the MX_2 composition Chemical Communications 51 8450-8453

[77] Ma Y, Liu B, Zhang A, Chen L, Fathi M, Shen C, Abbas A N, Ge M,

Mecklenburg M and Zhou C 2015 Reversible Semiconducting-to-Metallic Phase Transition in Chemical Vapor Deposition Grown Monolayer WSe$_2$ and Applications for Devices ACS Nano 9 7383-7391

[78] Schneider C, Glazov M M, Korn T, Höfling S and Urbaszek B 2018 Two-dimensional semiconductors in the regime of strong light-matter coupling *Nature Communications* 9 2695

[79] Lee M-K, Kim T G, Kim W and Sung Y-M 2008 Surface Plasmon Resonance (SPR) Electron and Energy Transfer in Noble Metal−Zinc Oxide Composite Nanocrystals The Journal of Physical Chemistry C 112 10079-10082

[80] Enyashin A N, Yadgarov L, Houben L, Popov I, Weidenbach M, Tenne R, Bar-Sadan M and Seifert G 2011 New Route for Stabilization of 1T-WS$_2$ and MoS$_2$ Phases The Journal of Physical Chemistry C 115 24586-24591

[81] Py M A and Haering R R 1983 Structural destabilization induced by lithium intercalation in MoS$_2$ and related compounds *Canadian Journal of Physics* 61 76-84

[82] Mattheiss L F 1973 Band Structures of Transition-Metal-Dichalcogenide Layer Compounds *Physical Review B* 8 3719-40

[83] Kang Y, Najmaei S, Liu Z, Bao Y, Wang Y, Zhu X, Halas N J, Nordlander P, Ajayan P M, Lou J and Fang Z 2014 Plasmonic Hot Electron Induced Structural Phase Transition in a MoS$_2$ Monolayer *Advanced Materials* 26 6467-71

[84] Jiménez Sandoval S, Yang D, Frindt R F and Irwin J C 1991 Raman study and lattice dynamics of single molecular layers of MoS$_2$ *Physical Review B* 44 3955-62

[85] Li Y, Zhou Z, Zhang S and Chen Z 2008 MoS$_2$ Nanoribbons: High Stability and Unusual Electronic and Magnetic Properties Journal of the American Chemical Society 130 16739-16744

[86] Livneh T and Sterer E 2010 Resonant Raman scattering at exciton states tuned by pressure and temperature in 2H-MoS$_2$ *Physical Review B* 81 195209